

Degree in Mathematics

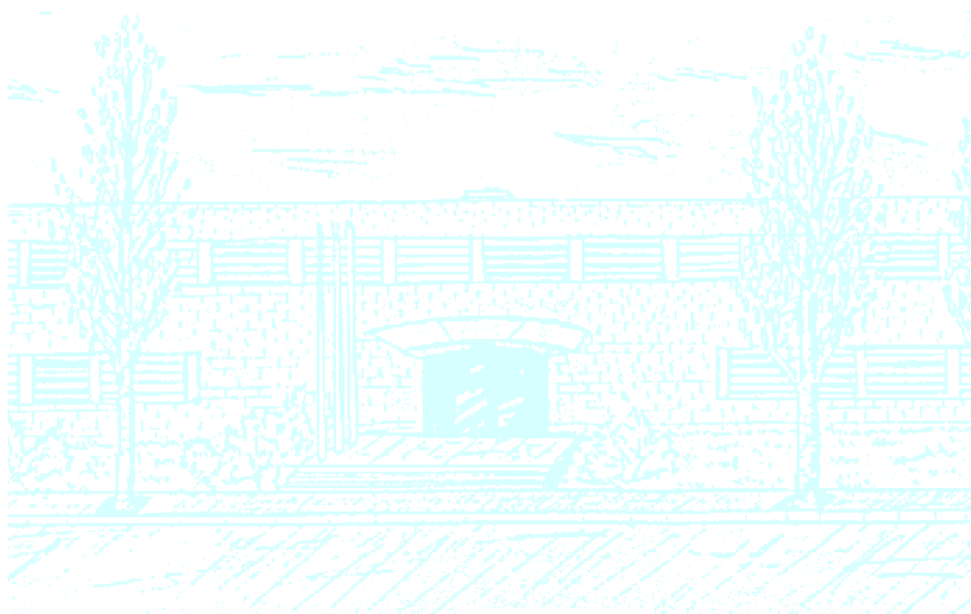
Title: Modelling relativistic effects in the light curves of tidal disruption events

Author: Júlia Alsina Oriol

Advisor: Tamara Bogdanović

Department: Center for Relativistic Astrophysics, School of Physics, Georgia Institute of Technology

Academic year: 2016-2017



UNIVERSITAT POLITÈCNICA DE CATALUNYA
BARCELONATECH

Facultat de Matemàtiques i Estadística

Universitat Politècnica de Catalunya
Facultat de Matemàtiques i Estadística

Degree in Mathematics
Bachelor's Degree Thesis

Modelling relativistic effects in the light curves of tidal disruption events

Júlia Alsina Oriol

Supervised by Tamara Bogdanović
Associate Professor of Physics, Georgia Institute of Technology

April, 2017

This project would not have been possible without the kind support and help of many individuals and organizations. I would like to express my gratitude to:

- CFIS and Fundació Privada Cellex, for giving me the opportunity to travel to Georgia Tech and for the financial support, within the CFIS Mobility Program.
- my advisor at Georgia Tech, Tamara Bogdanović, for her kindness, attention, guidance and support.
- Georgia Tech, for the facilities and the financial support to go to the 229th AAS Meeting, in Grapevine (Texas).
- my family and friends, especially Jordi and Jonás, who encouraged and motivated me to go to Georgia Tech and helped me before and during the trip.
- the people I met at Georgia Tech, especially Mary, for helping me to get used to the new environment, sharing their culture with me and making my trip more enjoyable.
- all the people who motivated and prepared me throughout my career: high school teachers, organizers of different activities I participated in (such as Mathematical Olympiads, Joves i Ciència, Kangourou sans Frontières), and UPC professors, among others.
- everybody that, directly or indirectly, contributed to make this possible.

Abstract

A star whose orbit takes it on a sufficiently close approach to a massive black hole (BH) will be shredded by the black hole's tides. Accretion of stellar debris on the BH gives rise to a characteristic light curve which has been used as a smoking gun in observational searches for tidal disruption events (TDEs) in the past 20 years. Disruptive encounters that occur very close to the MBHs are subject to relativistic effects, leading to an intriguing possibility that information about the space-time of an BH can be encoded in the light curve of a TDE. We explore the effect on the fallback rate of the general relativistic precession of the debris deep in the potential well of a Schwarzschild BH. We investigate the distribution of orbital energy of the debris in such scenarios and use it to assess the magnitude of relativistic effects that may be imprinted in the light curves of TDEs.

Keywords

black holes, tidal disruption, light curves, gravitation, general relativity

1. Introduction and objectives

Supermassive black holes (BHs) have been found to reside at the centers of most galaxies¹, often hosted within the nuclear star cluster of a host galaxy. As a consequence, there is a large number of stars orbiting these BHs, which interact gravitationally with the BH and each other through stochastic encounters. Occasionally, an encounter will shift a star onto an orbit close enough to the BH. Then, the star can be tidally disrupted and create an accretion disk around the BH, that results in a luminous X-ray flare. Figure 1 illustrates distribution of the debris around the BH after stellar disruption based on a hydrodynamic simulation of this scenario.

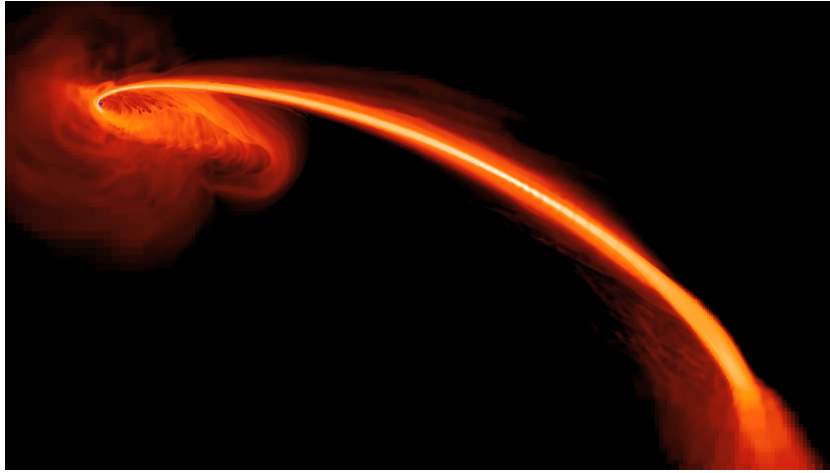


Figure 1: Snapshot from a simulation of a TDE illustrating distribution of the debris after stellar disruption. Location of the BH is marked by the blue dot, surrounded by the accretion disk. *Source:* <http://chandra.harvard.edu/photo/2012/ps1/>

The occurrence of TDEs was first explored in the 1970s as a possible way of fuelling active galactic nuclei (AGNs) [3], [5]. It was found that stellar concentrations around the BH needed to supply a quasar-level fuelling with TDEs were so great that other processes, such as stellar collisions would take place and release still more gas. This ruled out tidal disruptions as a leading mechanism to power quasars. Further investigation of the phenomenon itself was motivated by the first detections of tidal disruption candidates that took place in the 1990s. They have been used to detect the presence of massive black holes at the center of galaxies that were inactive before the flare. Specifically, if the source of a detected flare is at the center of the galaxy, as in Figure 2, and it exhibits a characteristic light curve associated with TDEs, this indicates that this likely is a location of a massive BH [7].

Tidal disruption events (TDEs) are not very common. Several works based on theoretical predictions and observations show that the rates of TDEs per BH range between once per 10,000 years to about once per million years [1], [4]. Early theoretical models of tidal disruptions predict light curves that decay with a characteristic time dependence $\propto t^{-5/3}$ [2], [3]. The study of the light curves from TDEs can provide information about the physical parameters of the disruption scenario. For example, the observed TDE light curves are commonly used to estimate the mass of the BH. The effects of general relativity may be important in vicinity of BHs, but are usually not taken into account when the light curves from TDEs are

¹The term supermassive black hole commonly refers to black holes with masses between $10^6 M_\odot$ and $10^9 M_\odot$.

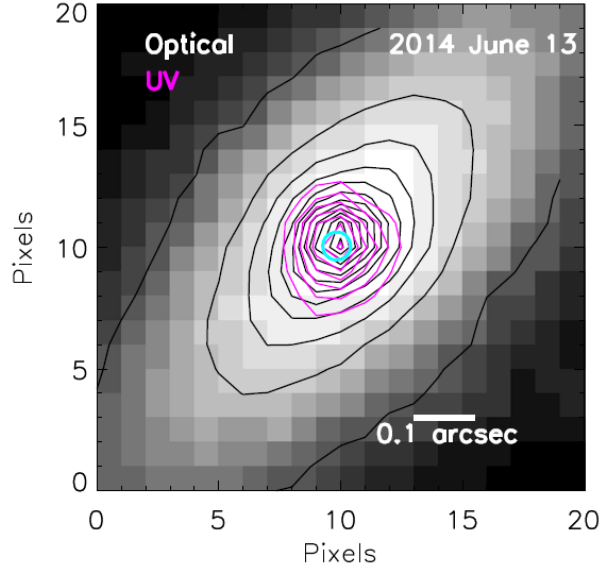


Figure 2: Image of tidal disruption event PS1-10jh. Grayscale and black contours show an optical image of the host galaxy. Magenta contours show the unresolved UV point source associated with the flare, which is coincident with the center of the galaxy. *Source: Gezari et al., 2015 [7].*

analysed and therefore, the estimated parameters can differ from the real ones.

This is the case because until very recently observations of tidal disruption candidates were relatively sparse and of insufficient cadence to allow discrimination between the non-relativistic and relativistic models. Along similar lines, a statistical sample of TDEs was until recently relatively small and on the order of two dozen, making a detection of a very close, relativistic tidal disruption unlikely. Both of these observational challenges have been addressed in the past few years with several new synoptic sky surveys that are monitoring the night sky for transients, such as TDEs and supernovae. The current and future transient surveys, such as Large Synoptic Survey Telescope (LSST), are expected to return high quality data from hundreds of TDEs per year. Since some of these may be results of relativistic encounters of stars with BHs, it is important to know whether they can be distinguished from non-relativistic TDEs.

In this project I will discuss relativistic effects that may be imprinted in light curves of TDEs. Using different models I have designed, I will present the relativistic signatures that can be seen in the light curves of TDEs and how they depend on different parameters, such as the mass of the BH, the strength of the encounter and the energy distribution after the disruption. Finally I will use the non-relativistic and relativistic models to estimate the mass of the BH from observational data of a particular TDE candidate (PS1-10jh).

2. Relevant parameters in TDEs

Newton's law of gravity states that particles attract each other with a force inversely proportional to the square of the distance between them. This implies that gravitational force exerted by one body on another is not constant across it if the interacting bodies have finite size (i.e., they are not point masses). This phenomenon can be observed in the tides of the oceans: there is a mutual attraction between the Moon and the Earth, but near oceans are more strongly attracted than further oceans, which result in tides.

The same effect can be also found in stars orbiting close to a BH. Let us consider a BH of mass M_{BH} and a star of mass m_* and radius R_* . The tidal radius (R_T) is defined as the distance from the BH to the star where the BH's tidal acceleration is approximately equal to the self-gravity of the star at its surface. Neglecting the inner structure of the star its self-gravity can be approximately described as

$$a_* = \frac{GM_*}{R_*^2}$$

The BH's acceleration at the closest point of the star's surface when the star is located at the tidal radius is given by

$$a_{BH} = \frac{GM_{BH}}{(R_T - R_*)^2} = \frac{GM_{BH}}{R_T^2} \frac{1}{(1 - R_*/R_T)^2} \approx \frac{GM_{BH}}{R_T^2} \left(1 + 2\frac{R_*}{R_T} + \dots\right)$$

Expanding the expression above into a Taylor series when $R_* \ll R_T$, a condition which is fulfilled for tidal disruptions of stars by massive black holes, gives the BH's tidal acceleration as

$$a_T \approx 2 \frac{GM_{BH}}{R_T^2} \frac{R_*}{R_T}$$

One can find the tidal radius by equating the star's self-gravity with the BH's tidal acceleration

$$R_T = pR_* \left(\frac{M_{BH}}{M_*}\right)^{1/3} \approx R_* \left(\frac{M_{BH}}{M_*}\right)^{1/3}$$

where p is a parameter of order unity that depends on the structure of the star. Specifically, this parameter encodes the fact that for two stars of equal mass and radius a more centrally concentrated star, with a compact core, will be more difficult to disrupt.

Let us consider a star coming from infinity, going on a parabolic orbit around a BH², with $R_P \approx R_T$, where R_P is the pericenter radius, i.e., the distance of closest approach to the BH. The velocity at the pericenter, before the disruption takes place, will be given by $v_p = \sqrt{2GM_{BH}/R_P}$. When the BH's tidal forces overcome the self-gravity of the star, it will be disrupted. Since the forces in distinct parts of the star are not the same, a torque is produced and, therefore, the star is spun up as it approaches the BH. Approximately half of the debris mass from a spinning star will be flung towards the BH and will remain bound to it, and the other half will be unbound and launched away from the BH (see Figure 3). The bound debris will initially occupy very eccentric orbits. As debris returns toward the BH for the subsequent pericentric passage the orbits will intersect and produce an accretion disk.

Note that for the most massive black holes the tidal radius of the star falls within the event horizon of the black hole, $R_T < R_s = 2GM_{BH}/c^2$. Assuming a non-rotating BH this sets a limit on the mass of BHs

²Note that other types of orbits are also allowed but nearly parabolic orbits are expected to be most probable, given that larger fraction of stars reside in a larger volume about the BH.

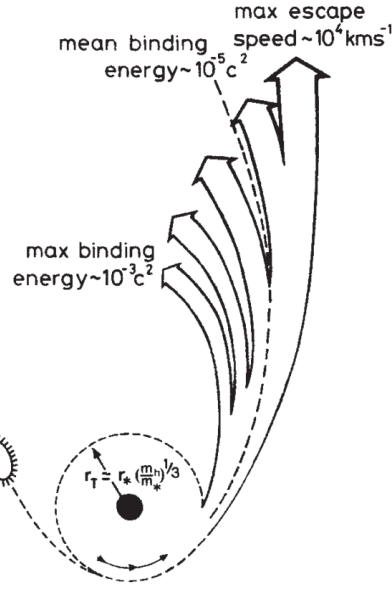


Figure 3: Sketch showing a tidal disruption of a star. *Source: Rees, 1998 [3].*

that can disrupt solar-type stars as $M_{BH} \lesssim 10^8 M_{\odot}$. In the case of more massive BHs, the star falls into the event horizon before it is disrupted and fails to produce luminous flare which is a key signature of tidal disruptions.

The strength of the encounter β can be defined as the relation between the tidal radius R_T and the pericenter radius R_P of the star's initial orbit:

$$\beta = \frac{R_T}{R_P}$$

It follows that the larger the value of β , the stronger the tidal encounter. Tidal interaction characterized by $\beta \lesssim 1$ are considered as weak or partial disruptions, in which the star is not completely disrupted and the core of the star can survive (see Figure 4).

2.1 Energy spread of the debris bound to the BH

Initially, a star on a parabolic orbit has orbital energy $E = 0$. After the disruption, each mass element of the debris will have a different energy, as about a half of mass elements will end up on bound orbits ($E < 0$) and the remainder on unbound orbits ($E > 0$) as described above. Let us find an approximate expression to describe the spread in energy of debris material that after disruption ends up bound to the BH, relative to the initial parabolic orbit of the star. This energy spread will allow us to estimate a range of orbits that the debris will occupy after disruption as well as its proximity to the BH.

For a debris mass element with the orbital speed v , the specific orbital energy will be $\epsilon = \frac{1}{2}v^2 + \Phi(r)$, where $\Phi(r) = -\frac{GM_{BH}}{r}$ is the BH potential. Calculating the energy spread for the point on the star that

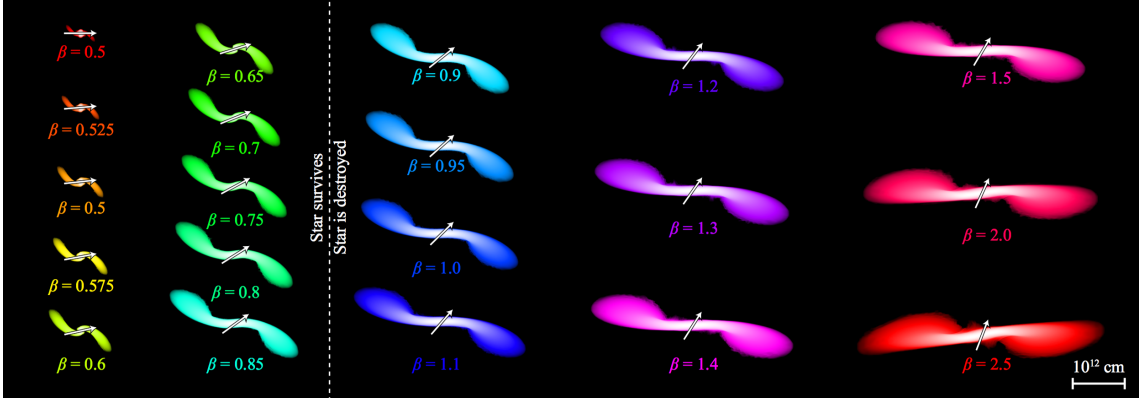


Figure 4: Snapshots from several simulations of tidal disruptions shortly after the star is tidally disrupted. The arrows show the location toward the BH. For large β the star is completely destroyed, while for small β the star loses the outer layers but its core survives. *Source: Guillochon and Ramirez-Ruiz, 2013 [15].*

is located deepest in the potential well of the BH and the point at the center of the star one finds

$$\Delta\epsilon = \epsilon_{\text{center}} - \epsilon_{\text{closest}} = \Phi(R_P) - \Phi(R_P - R_*)$$

Expanding the BH potential into a Taylor series,

$$\Phi(R_P - R_*) \approx \Phi(R_P) + \Phi'(R_P)R_*$$

and therefore,

$$\Delta\epsilon = \Phi(R_P) - \Phi(R_P - R_*) \approx -\Phi'(R_P)R_* = \frac{GM_{BH}}{R_P} \frac{R_*}{R_P}$$

The following approximations have been used to obtain this formula: (a) we consider an instantaneous disruption of the star once it arrives to the pericenter of its orbit (in reality the star starts experiencing BH tides at a larger distance) and (b) we neglect the effects of internal structure of the star.

2.2 Newtonian orbits

It is known that in a two body problem, which considers gravitational interaction of the two point masses, the motion of one body relative to another will lie in a plane. Since in our system the BH is many orders of magnitude more massive than the star, we can consider the BH resides at rest in the center of mass of the binary system. In the spherical-polar coordinate system defined by coordinates (r, θ, ϕ) we can place the BH at the coordinate origin and the orbit of the star in the plane $\theta = \pi/2$. Here, θ measures the angle from the tip of the vector of orbital angular momentum to the plane of the binary.

In this setup the coordinates of the star are $x = r \cos \phi$ and $y = r \sin \phi$, and hence its speed is given by $v^2 = \dot{x}^2 + \dot{y}^2 = \dot{r}^2 + r^2 \dot{\phi}^2$. It is not difficult to see that the specific energy $\epsilon = \frac{1}{2}(\dot{r}^2 + r^2 \dot{\phi}^2) + \frac{GM_{BH}}{r}$ and the specific orbital angular momentum $l = r^2 \dot{\phi}$ are conserved.

Since we are interested in the debris bound to the BH we will only consider orbits with $\epsilon < 0$. For elliptical orbits characterized by the semi-major axis a and eccentricity e the pericenter and apocenter of

the orbit are $r_p = a(1 - e)$ and $r_a = a(1 + e)$, respectively. Evaluating

$$\epsilon = -\frac{GM_{BH}}{r} + \frac{1}{2} \left(\dot{r}^2 + \frac{l^2}{r^2} \right)$$

at these two points, where $\dot{r} = 0$, it is easy to find that $\epsilon = -\frac{GM}{2a}$ and $l^2 = GMa(1 - e^2)$. Replacing the expressions for ϵ and l^2 , with the orbital parameters

$$\left(\frac{dt}{dr} \right)^2 = \frac{1}{2\epsilon + \frac{2GM_{BH}}{r} - \frac{l^2}{r^2}} = \frac{a}{GM_{BH}} \frac{r^2}{a^2 e^2 - (r - a)^2}$$

Since $r \in [r_p, r_a] = [a(1 - e), a(1 + e)]$, we can introduce the variable ξ , such that $r = a(1 - e \cos \xi)$ and

$$\left(\frac{dt}{d\xi} \right)^2 = \left(\frac{dt}{dr} \frac{dr}{d\xi} \right)^2 = \frac{a}{GM} \frac{a^2(1 - e \cos \xi)^2}{a^2 e^2 - a^2 e^2 \cos^2 \xi} a^2 e^2 \sin^2 \xi = \frac{a^3}{GM_{BH}} (1 - e \cos \xi)^2$$

which gives us the equation

$$\frac{dt}{d\xi} = \sqrt{\frac{a^3}{GM}} (1 - e \cos \xi)$$

Integrating this equation from $\xi = 0$ to $\xi = 2\pi$, we can find the orbital period of the debris element with the semi-major axis a , which corresponds to the Kepler's third law.

$$\tau = 2\pi \sqrt{\frac{a^3}{GM_{BH}}}$$

2.3 Mass accretion rate of stellar debris and accretion powered light curves

The recent, high quality observational data shows that optical light curves of TDEs are quite complex and characterized by source-by-source variations that are not captured by the canonical $L \propto t^{-5/3}$ model, mentioned in the introduction. The differences are thought to arise from intrinsic variations in the type of the disrupted star, its initial orbit but also, due to reprocessing of the ionizing photons that emerge from the debris accretion disk by the surrounding medium. This latter effect of radiation transport is perhaps the most complex of all and is only beginning to be addressed in theoretical models in this stage. At the time of this writing, no computational models of tidal disruption events are self-consistently accounting for reprocessing of radiation by the debris because such simulations are prohibitively computationally expensive. Instead, theoretical models commonly evaluate the accretion onto the BH and conjecture that accretion powered luminosity will remain approximately proportional to the accretion rate as a function of time, if the effects of absorption and re-emission of emitted radiation are not significant. We adopt this approximation here and assume that the luminosity of a TDE is proportional to the return rate of debris mass to the pericenter.

$$L = \mu \dot{M} c^2$$

with $\mu \approx 0.1$. The return rate of debris mass to the pericenter is given by

$$\dot{M} = \frac{dM_*}{d\tau} = \frac{dM_*}{d\epsilon} \frac{d\epsilon}{d\tau}$$

where the first term represents the distribution of the debris mass over the specific orbital energy and it is often assumed to be uniform [2] so that

$$\frac{dM_*}{d\epsilon} = \frac{M_*}{2\Delta\epsilon}$$

where the factor of “2” accounts for both the bound and unbound half of the star after the disruption. Actually, distributions of debris mass over specific energy in TDE are more complex and depart from uniform distribution as soon as the debris streams start to intersect and exchange energy, shortly after the star is disrupted. In relativistic stellar disruptions, intersection of orbits is even more pronounced and driven by the relativistic precession of the orbits. How the shape of this distribution affects to the shape of the light curves will be shown in more detail in Section 2.5

The second term in the expression for \dot{M} can be evaluated using the expression for the Keplerian orbital period,

$$\tau = 2\pi\sqrt{\frac{a^3}{GM_{BH}}} = -\frac{\pi GM_{BH}}{\sqrt{2|\epsilon|^3}} \Rightarrow \epsilon = -\left(\frac{\pi GM_{BH}}{\sqrt{2}\tau}\right)^{2/3}$$

where the relation $\epsilon = -\frac{GM_{BH}}{2a}$ has been used. Therefore,

$$\frac{d\epsilon}{d\tau} = \frac{1}{3}(2\pi GM_{BH})^{2/3}\tau^{-5/3}$$

Assuming a uniform distribution of the debris over orbital energy, the return rate of debris to the pericenter can be determined to be

$$\dot{M} = \frac{M_*}{2\Delta\epsilon} \frac{1}{3}(2\pi GM_{BH})^{2/3}\tau^{-5/3} = \frac{1}{3} \frac{M_*}{\tau_m} \left(\frac{\tau}{\tau_m}\right)^{-5/3}$$

where $\tau_m = \frac{\pi}{\sqrt{2GM_{BH}}} \frac{R_P^3}{R_*^{3/2}}$ corresponds to the period of the most strongly bound debris, characterized by specific orbital energy $-\Delta\epsilon$. The most strongly bound debris elements occupy orbits located deepest in the potential well of the BH characterized by the shortest orbital periods. Therefore, these debris elements are the first to return to the pericenter of the orbit after disruption, where they form an accretion disk and fall into the BH.

2.4 A particular scenario

To give an idea of the orders of magnitude, let us consider a BH of mass $M_{BH} = 10^6 M_\odot$ and a solar-type star ($M_* = 1 M_\odot$ and $R_* = 1 R_\odot$) going on a parabolic orbit around the BH, where $R_\odot \approx 6.955 \cdot 10^{10}$ cm and $M_\odot \approx 1.989 \cdot 10^{33}$ g are the radius and mass of the Sun. We assume it is a tidal disruption event with strength parameter $\beta = 1$. It is also useful to define the gravitational radius $R_g = GM_{BH}/c^2$. It is related to Schwarzschild radius $R_s = 2R_g$, which defines the event horizon of non-spinning BHs.

In this scenario, $R_g = 1.477 \cdot 10^{11}$ cm and $R_P = R_T \approx 6.955 \cdot 10^{12}$ cm $= 47.1 R_g$. At the pericenter, the star will have a velocity of $v_P = 6.175 \cdot 10^9$ cm/s $= 6.175 \cdot 10^4$ km/s. Assuming that the most strongly bound debris has specific orbital energy $-\Delta\epsilon = -1.907 \cdot 10^{17}$ erg/g, the accretion onto the BH will start upon the return of this debris to the pericenter of its orbit, $\tau_m = 3.543 \cdot 10^6$ s $= 0.112$ years after the disruption takes place. The orbital semi-major axis of the most bounded fluid element will be $a_m = 3.4775 \cdot 10^{14}$ cm $= 2.354 \cdot 10^3 R_g \gg R_P$. Given the value of the pericenter of the original orbit, the eccentricity can be found to be $e = 0.98$, indicating that the orbits of the debris are very eccentric.

2.5 Energy distribution shapes

The accretion rate curve sensitively depends on the distribution of specific orbital energy across the star after the disruption. This is illustrated in Figure 5 which shows different energy distributions of the debris and the corresponding accretion rate curves. The blue lines in the upper plots show the flat energy distribution, discussed in Section 2.3.

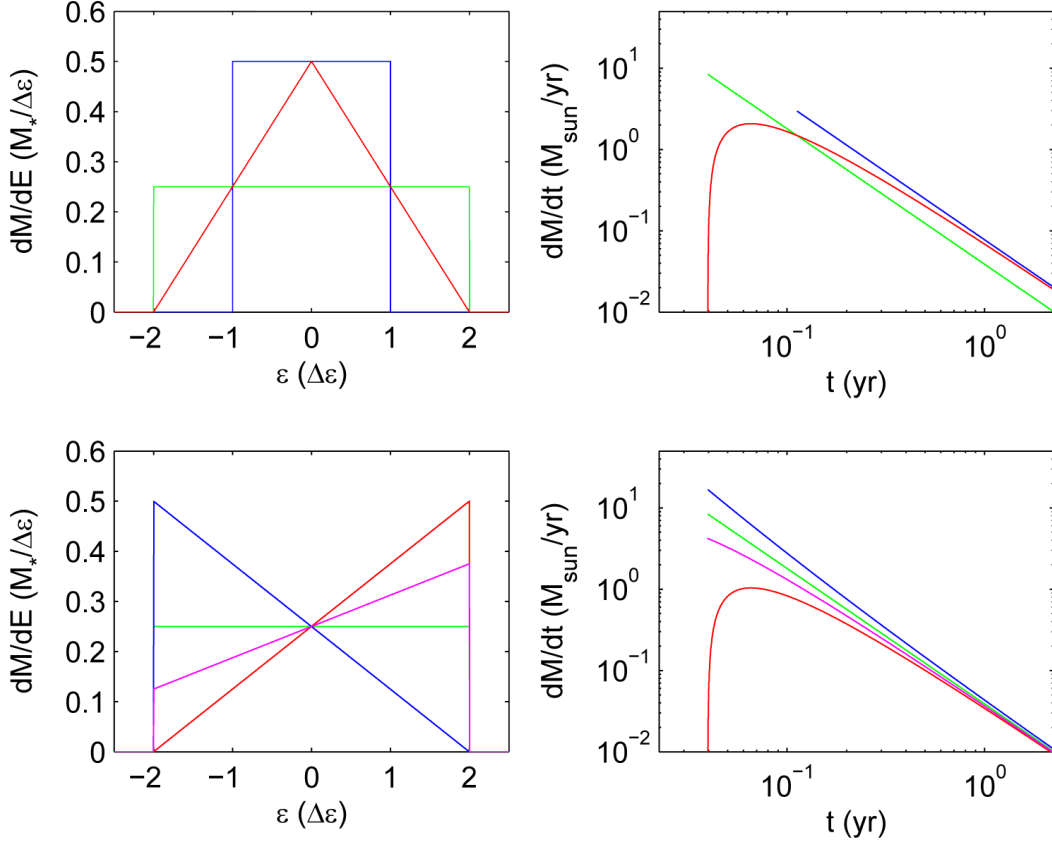


Figure 5: Energy distributions (left) and the corresponding accretion rate curves (right), for a scenario with $M_{BH} = 10^6 M_{\odot}$, $M_* = M_{\odot}$, $R_* = R_{\odot}$ and $R_P = R_T = R_*(M_{BH}/M_*)^{1/3}$.

It can be observed that:

- For flat distributions, the accretion rate curve is proportional to $t^{-5/3}$, consistent with the canonical model for TDEs. In wider energy distributions the debris elements that are more strongly bound to the BH (and have shorter periods) start being accreted earlier than the debris elements characterized by narrower distributions.
- For distributions with a larger fraction of bound mass debris (blue line in the lower plots), the accretion rate curves are steeper than the flat energy distribution. For distributions with less bound mass debris (red and magenta lines in the lower plots), the accretion rate curves are below the flat energy distribution scenario.
- Both red distributions give rise to the same shape of the accretion rate curve but have somewhat

different amplitude. This is because the only difference between the two distributions is the total amount of debris mass bound to the BH ($\epsilon < 0$) – since the red energy distribution in the bottom panel has a smaller fraction of mass bound to the BH, the resulting accretion rate appears scaled down in amplitude from the top panel red distribution.

3. Relativistic effects

General theory of relativity was published in 1915 by Albert Einstein. It is a geometric theory of gravitation which generalizes special relativity and Newton's law of universal gravitation, providing a unified description of gravity as a geometric property of spacetime.

The Schwarzschild metric is a solution to the Einstein field equations that describes the spacetime outside a non-rotating and uncharged spherical mass. A line element in this metric is given by

$$ds^2 = \left(1 - \frac{R_s}{r}\right) c^2 dt^2 - \left(1 - \frac{R_s}{r}\right)^{-1} dr^2 - r^2 d\theta^2 - r^2 \sin^2 \theta d\phi^2$$

where $R_s = \frac{2GM_{BH}}{c^2}$ is called the Schwarzschild radius [8].

The metric is given by

$$g_{\alpha,\beta} = \begin{pmatrix} -(1 - R_s/r) & 0 & 0 & 0 \\ 0 & (1 - R_s/r)^{-1} & 0 & 0 \\ 0 & 0 & r^2 & 0 \\ 0 & 0 & 0 & r^2 \sin^2 \theta \end{pmatrix}$$

It can be shown that in this metric, the quantities $e = \left(1 - \frac{R_s}{r}\right) \frac{dt}{d\tau}$ and $\ell = r^2 \sin^2 \theta \frac{d\phi}{d\tau}$, which are the energy and the angular momentum per unit rest mass, respectively, are conserved. Since the angular momentum is conserved, the orbits lie in a plane. Reorienting the coordinates we can assume $\theta = \pi/2$.

From the normalization of the four-velocity it can be obtained that $u^\alpha u_\alpha = g_{\alpha\beta} u^\alpha u^\beta = -c^2$. Therefore,

$$-u_t^2(1 - R_s/r) + u_r^2(1 - R_s/r)^{-1} + u_\phi^2 r^2 = -c^2$$

Using that $u_t = \frac{dt}{d\tau}$, $u_r = \frac{dr}{d\tau}$ and $u_\phi = \frac{d\phi}{d\tau}$, and replacing by e and ℓ we obtain

$$e^2 \left(1 - \frac{R_s}{r}\right)^{-1} + \left(\frac{dr}{d\tau}\right)^2 \left(1 - \frac{R_s}{r}\right)^{-1} + \frac{\ell^2}{r^2} = -c^2$$

Defining $\mathcal{E} = \frac{e^2 - 1}{2}$, the previous formula can be written as

$$\mathcal{E} = \frac{1}{2} \left(\frac{dr}{d\tau}\right)^2 + V_{\text{eff}}(r)$$

where

$$V_{\text{eff}}(r) = \frac{1}{c^2} \left(-\frac{GM_{BH}}{r} + \frac{\ell^2}{2r^2} - \frac{GM_{BH}\ell^2}{c^2 r^3} \right)$$

is the relativistic effective potential.

Since the relation between e and the usual Newtonian specific energy ϵ_N is given by $e = 1 + \frac{\epsilon_N}{c^2}$, we get that

$$\epsilon_N + \frac{\epsilon_N^2}{2c^2} = \frac{1}{2} \left(\frac{dr}{d\tau}\right)^2 + \frac{\ell^2}{2r^2} - \frac{GM_{BH}}{r} - \frac{GM_{BH}\ell^2}{c^2 r^3}$$

This will allow us to calculate parameters of interest, such as the period of the orbits and the pericenter precession.

3.1 Scenarios of interest

When there is an encounter between a star and a BH, different outcomes can happen depending on the initial scenario, as it is shown in Figure 6. TDEs take place inside the triangle in the figure. The base of the triangle is given by $\beta = 1$, i.e., $R_P = R_T$. If the pericenter radius is greater than the tidal radius there is no (complete) disruption of a star. On the right, outside the triangle, the pericenter is too small, and hence, the star falls into the BH before disrupting. The limiting line is $R_P = R_s = 2R_g$ for non-spinning BH and $R_P = R_s = R_g$ for maximally spinning BHs. Finally, on the left, the radius of the star is bigger than the pericenter radius and therefore, the BH enters the star.

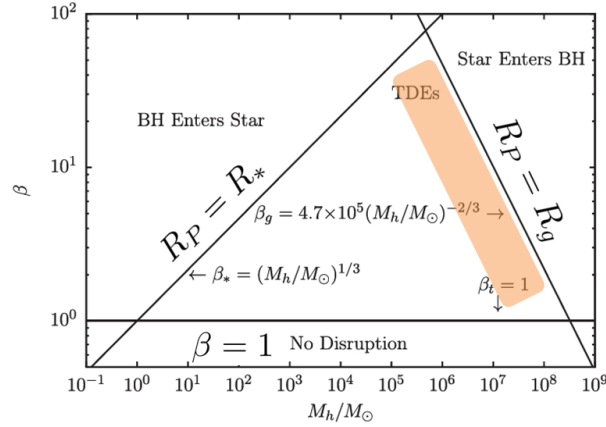


Figure 6: Illustration of disruption regimes for a solar-type star. *Source: Evans, Laguna and Eracleous, 2015 [11].*

3.2 Effects on the energy distribution

Once the star, which is originally in a parabolic orbit, gets close enough to the pericenter of the orbit (assuming $R_P = R_T$), the tidal forces produced by the BH will disrupt the star, resulting in a distribution of debris mass over specific orbital energy. This distribution depends on the structure of the star (see Section 4). For negative energies (bound debris) we will initially consider a flat distribution of width $\sigma_{E,N}$, with an exponential decay at the edge, defined by some parameter $\alpha > 0$. For the newtonian model, the distribution will be given by:

$$\frac{dM}{d\epsilon}(\epsilon) = \begin{cases} Ae^{\alpha(\epsilon + \sigma_{E,N})/\Delta\epsilon} & \text{if } \epsilon < -\sigma_{E,N} \\ A & \text{if } -\sigma_{E,N} \leq \epsilon \leq \sigma_{E,N} \\ Ae^{-\alpha(\epsilon - \sigma_{E,N})/\Delta\epsilon} & \text{if } \epsilon > \sigma_{E,N} \end{cases}$$

where

$$A = \frac{M_*/2}{\Delta\epsilon/\alpha + \sigma_{E,N}}$$

Note that the shape for positive energies will not affect to the accretion rate as long as the condition

$$\int_{-\infty}^{\infty} \frac{dM}{d\epsilon} d\epsilon = M_*$$

is fulfilled.

A star having a close encounter with a BH will experience stronger tides in the relativistic than newtonian gravitational potential. Therefore, the spread in the specific orbital energy accross the star will be larger in the relativistic model. According to Servin and Kesden (2016) [10], the width of the debris energy distribution after the disruption in general relativity evaluated at the pericenter for encounters with $\beta \leq 1$ (partial disruptions) is given by

$$\sigma_{E,GR,PD} = \frac{M_{BH}R_*}{R_P^2} \left(1 - \frac{2M_{BH}}{R_P}\right)^{-1/2}$$

and the width of the debris energy for a Newtonian orbit with the same pericenter will be given by

$$\sigma_{E,N,PD} = \frac{M_{BH}R_*}{R_P^2}$$

Therefore, the relation between the widths in both models will be given by

$$\sigma_N/\sigma_{GR} = \sqrt{1 - \frac{2M_{BH}}{R_P}}$$

In this project it will be assumed that this expansion in the energy distribution is linear, so we will rescale the energy by this factor. Therefore, the debris element that has specific energy ϵ_N in the newtonian model, will have specific energy $\epsilon_{GR} = \epsilon_N \frac{\sigma_{GR}}{\sigma_N}$ in the relativistic model. The factor A will need to change to ensure the total mass is M_* . The plot of the distribution for the newtonian and relativistic models, using $\alpha = 3$ is given in Figure 7.

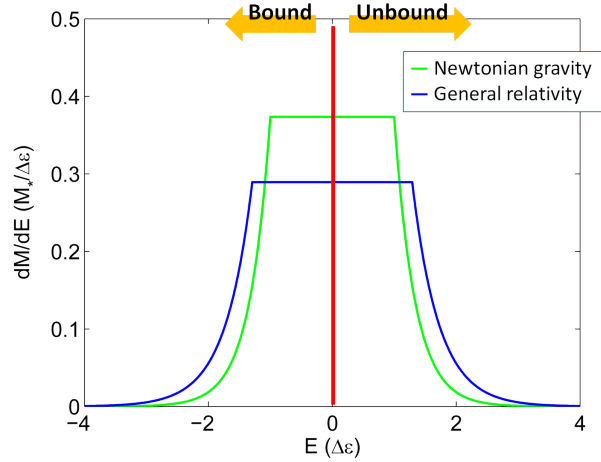


Figure 7: Distribution of the debris mass over specific orbital energy, for a star disrupted in a Newtonian (green) and relativistic (blue) gravitational potential of a BH. Parameters of the encounter: $M_{BH} = 10^7 M_\odot$, $M_* = M_\odot$, $R_* = R_\odot$, $R_P = R_T = 5 R_g$.

3.3 Effects on the precession of the pericenter

In general relativity the gravitational force departs from the $\propto 1/r^2$ law in vicinity of the BH, resulting in a relativistic precession of the pericenter of the orbit. Note that an additional relativistic effect that

arises around *spinning* black holes is the precession of the orbital plane about the BH spin axis. Since we focus on non-spinning BHs in this thesis, we neglect the effect of precession of the debris orbital plane (see Figure 8).

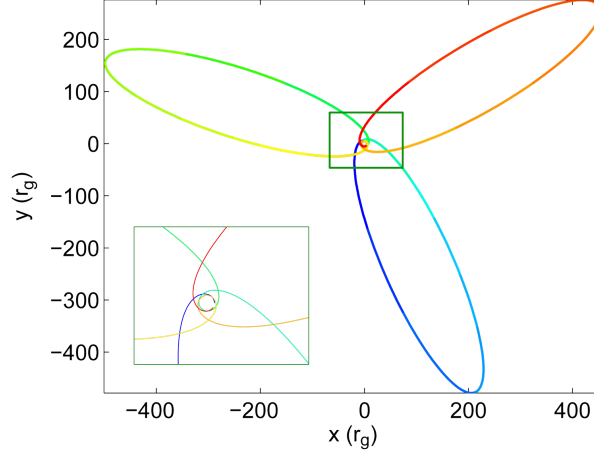


Figure 8: Orbits for bound debris in the scenario in Figure 7, showing the precession of the pericenter (about $228^\circ/\text{orbit}$). Inset shows the zoom-in view of the central region.

For relativistic effects in the weak field regime, the precession of the pericenter per revolution (i.e., one complete orbit) is given by

$$\Delta\varphi = \frac{6\pi GM_{BH}}{c^2(1-e^2)a}$$

where a and e are the semi-major axis and eccentricity of the orbit. When relativistic effects are more important, in the strong field regime (i.e., within few R_g from the event horizon), this formula is no longer valid. Then, the expression derived below needs to be used. Starting from

$$\left(\frac{dr}{d\tau}\right)^2 = 2\epsilon_N + \frac{\epsilon^2}{c^2} + \frac{2GM_{BH}}{r} - \frac{\ell^2}{r^2} + \frac{2GM_{BH}\ell^2}{c^2 r^3}$$

and defining

$$u = \frac{2}{r}$$

we get that

$$\begin{aligned} \left(\frac{du}{d\phi}\right)^2 &= \left(\frac{du}{dr}\right)^2 \left(\frac{dr}{d\tau}\right)^2 \left(\frac{d\tau}{d\phi}\right)^2 = \frac{4}{r^4} \left(2\epsilon_N + \frac{\epsilon_N^2}{c^2} + GM_{BH}u - \frac{\ell^2 u^2}{4} + \frac{GM_{BH}\ell^2 u^3}{4c^2}\right) \frac{r^4}{\ell} \\ &= \frac{GM_{BH}}{c^2} \left(u^3 - \frac{c^2}{GM_{BH}}u^2 + \frac{4c^2}{\ell^2}u + \frac{8\epsilon_N c^2}{GM_{BH}\ell^2} + \frac{4\epsilon_N^2}{GM_{BH}\ell^2}\right) = \frac{GM_{BH}}{c^2}(u-u_1)(u-u_2)(u-u_3) \end{aligned}$$

where $u_1 = \frac{2}{r_p}$, $u_2 = \frac{2}{r_a}$ and u_3 are the roots of the polynomial, and r_p and r_a the pericenter and apocenter, respectively.

Along the orbit, u oscillates from u_1 to u_2 . We use $u = \mu(1 + \varepsilon \cos \alpha)$, where $\alpha \in [0, 2\pi]$. Then, $u_1 = \mu(1 + \varepsilon)$ and $u_2 = \mu(1 - \varepsilon)$, and therefore $\mu = \frac{u_1 + u_2}{2}$ and $\varepsilon = \frac{u_1 - u_2}{u_1 + u_2}$.

It is known (using Viète's formulas) that $u_1 + u_2 + u_3 = \frac{c^2}{GM_{BH}}$. Therefore,

$$(u - u_1)(u - u_2)(u - u_3) = -\mu^2 \varepsilon^2 \sin^2 \alpha \left(3\mu + \mu \varepsilon \cos \alpha - \frac{c^2}{GM_{BH}} \right)$$

To calculate the precession we will need to integrate $\frac{d\alpha}{d\phi}$ for an orbit. We know

$$\left(\frac{d\alpha}{d\phi} \right)^2 = \left(\frac{d\alpha}{du} \right)^2 \left(\frac{du}{d\phi} \right)^2 = \frac{1}{\mu^2 \varepsilon^2 \sin^2 \phi} \frac{GM_{BH}}{c^2} (u - u_1)(u - u_2)(u - u_3) = 1 - 3r_g \mu - r_g \mu \varepsilon \cos \alpha$$

where $r_g = \frac{G_{BH}}{c^2}$. Therefore,

$$\Delta\phi = 2 \int_0^\pi (1 - 3r_g \mu - r_g \mu \varepsilon \cos \alpha)^{-1/2} d\alpha$$

The precession is given by $\Delta\varphi = \Delta\phi - 2\pi$. Using Taylor expansion and integrating we can easily obtain

$$\Delta\varphi \approx 3\pi r_g \mu + \left(\frac{27}{4} + \frac{3}{8} \varepsilon^2 \right) \pi r_g^2 \mu^2 + \dots$$

where $\mu = \frac{u_1 + u_2}{2} = \frac{1}{r_a} + \frac{1}{r_p}$ and $\varepsilon = \frac{r_a - r_p}{r_a + r_p}$.

Taking the first term and using the newtonian formulas for the pericenter and apocenter, $r_p = a(1 - e)$ and $r_a = a(1 + e)$ we recover the result

$$\Delta\varphi = \frac{6\pi GM_{BH}}{c^2 a(1 - e^2)}$$

Therefore, since in relativistic potential the debris orbit spans more than 2π , it is expected that the time required for the debris mass to return to the pericenter for the second time will be larger in the relativistic model than in the Newtonian model.

As it has been calculated in Section 2.2, the period in the newtonian model is:

$$t_N = 2\pi \sqrt{\frac{a^3}{GM}}$$

In the relativistic model we know that

$$\frac{dr}{d\tau} = \pm \sqrt{2\epsilon_N + \frac{\epsilon_N^2}{c^2} + \frac{2GM_{BH}}{r} - \frac{\ell^2}{r^2} + \frac{2GM_{BH}\ell^2}{c^2 r^3}}$$

and

$$\frac{dt}{d\tau} = e \left(1 - \frac{R_s}{r} \right)^{-1} = \left(1 + \frac{\epsilon_N}{c^2} \right) \left(1 - \frac{R_s}{r} \right)^{-1}$$

To obtain the period, we need to integrate $\frac{dt}{dr} = \frac{dt}{d\tau} \frac{d\tau}{dr}$ for an orbit of the debris mass. From r_p to r_a , since the radius increases, the correct formula will have the positive sign. From r_a to r_p , the valid sign will be the negative one. Therefore,

$$t_{GR} = 2 \int_{r_p}^{r_a} \left(1 + \frac{\epsilon_N}{c^2} \right) \left(1 - \frac{R_s}{r} \right)^{-1} \left(2\epsilon_N + \frac{\epsilon_N^2}{c^2} + \frac{2GM_{BH}}{r} - \frac{\ell^2}{r^2} + \frac{2GM_{BH}\ell^2}{c^2 r^3} \right)^{-1/2} dr$$

In the newtonian development we used that $r_a = a(1 + e)$ and $r_p = a(1 - e)$, but these formulas are not true in the relativistic model. In order to find the values of r_a and r_p we will need to solve the equation $\frac{dr}{dt} = 0$. Since $\frac{dr}{dt} = \frac{dr}{d\tau} \frac{d\tau}{dt}$ and $\frac{d\tau}{dt} = 0$ only when $r = R_s$ (event horizon), we need to solve $\frac{dr}{d\tau} = 0$, and hence r_a and r_p are the two largest solutions of

$$\left(2\epsilon_N + \frac{\epsilon_N^2}{c^2}\right) r^3 + 2GM_{BH}r^2 - \ell^2 r + \frac{2GM_{BH}\ell^2}{c^2} = 0$$

Note that, although the specific orbital angular momentum was not important to calculate t_N , it will be needed to calculate t_{GR} , precisely because the amount of precession of the pericenter depends on angular momentum. Therefore, we need to know the spread in orbital momentum after the disruption. According to Servin and Kesden (2016) [10], the spread in specific orbital momentum after the disruption for a partial disruption with $\beta \leq 1$ is given by

$$\sigma_{\ell,GR,PD} = \ell_p \left(\frac{M_*}{M_{BH}}\right)^{1/3} \left(\frac{R_T}{R_P}\right)^{1/2}$$

where $\ell_p = R_p \gamma(v_p) v_p$ is the orbital momentum of the initial parabolic orbit, and $\gamma(v) = 1/\sqrt{1 - v^2/c^2}$.

In the scenario from Figure 7, we compare the time required for debris mass of specific energy $\epsilon = -\Delta\epsilon \approx -1.693 \cdot 10^{18} \text{ erg/g}$ to complete an orbit. The period will be $t_N \approx 15.5$ days for the Newtonian model and $t_{GR} \approx 15.6$ days for the relativistic model. The difference between the two models is small (less than 1%) and hence, it is expected that the effects due to the precession of the pericenter will be small. The periods for the relativistic model using specific orbital momentums ℓ_T and $\ell_T \pm \sigma_{\ell,GR,PD}$ are negligible (less than 0.01%).

The accretion rates obtained for both models in this scenario are shown in Figure 9 and will be discussed in detail in Section 5.

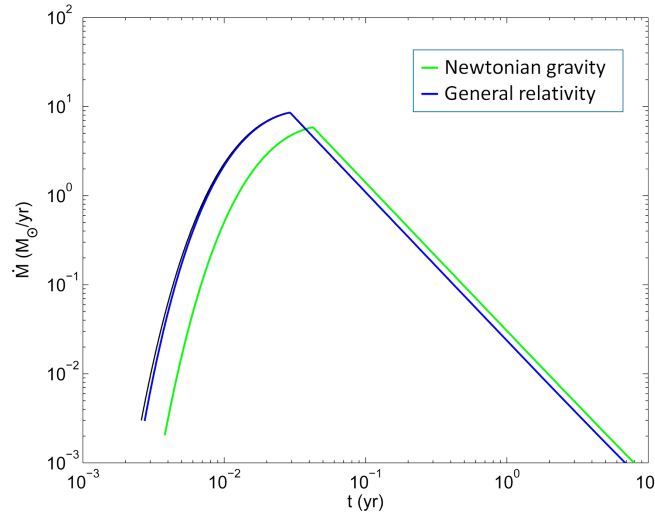


Figure 9: Accretion rate curves obtained in the scenario in Figure 7, for both newtonian and relativistic models.

4. Stellar structure

Models presented in the previous sections assume that the stellar debris after disruption has uniform distribution over orbital energies, which decays exponentially at the distribution edges. More realistically, the initial energy distribution of the debris is imprinted by the binding energy of the star and thus depends on the internal structure of the star, such as its density and pressure profile. As discussed in Section 2.5, the shape of the energy distribution determines the shape of the light curve. In this section we examine the effect of the stellar structure on the resulting TDE light curve by taking into account the internal structure of a disrupted star.

4.1 Lane-Emden equation

A structure of a spherical star in hydrostatic equilibrium can be described by the following equations:

$$\frac{dP}{dr} = -\frac{GM}{r^2}\rho$$

$$\frac{dM}{dr} = 4\pi r^2 \rho$$

where M is the total stellar mass enclosed within the radius r measured from the center of the star. Combining these two equations we obtain

$$\frac{1}{r^2} \frac{d}{dr} \left(\frac{r^2}{\rho} \frac{dP}{dr} \right) = -4\pi G \rho$$

We assume that the relationship between the pressure and density within the star can be described by the polytropic equation of state

$$P = K\rho^\gamma$$

where K is the polytropic constant and γ is the adiabatic index. Using the polytropic equation of state and defining radius and density in terms of dimensionless properties as $r = \alpha\xi$ and $\rho = \rho_c\theta^n$, where ρ_c is the density at the center and $n = \frac{1}{\gamma-1}$ is the polytropic index, we obtain that

$$\frac{K\rho_c^{1/n}}{\alpha\xi^2} \frac{d}{d\xi^2} \left(\frac{\xi}{\theta^n} \frac{d(\theta^{n+1})}{d\xi} \right) = -4\pi G \rho_c \theta^n$$

Defining the length scale α as

$$\alpha^2 = \frac{(n+1)K\rho_c^{\frac{1}{n}-1}}{4\pi G}$$

and using

$$\frac{d(\theta^{n+1})}{d\xi} = (n+1)\theta^n \frac{d\theta}{d\xi}$$

we obtain the Lane-Emden equation:

$$\frac{1}{\xi^2} \left(\xi^2 \frac{d\theta}{d\xi} \right) = -\theta^n$$

This equation can be solved numerically beginning at the star's center ($\xi = 0$), where $\theta(0) = 1$ and $\theta'(0) = 0$. One needs to integrate to the star's surface, ξ_1 , defined as the smallest $\xi > 0$ such that $\theta(\xi) = 0$. Note that the equation exhibits a singularity at $\xi = 0$. A strategy to solve that is to develop a power series expansion at this point in order to find initial conditions for a small positive ξ , using the relations given by the Lane-Emden equation. The Taylor expansion for $\theta(\xi)$ is given by:

$$\theta(\xi) = 1 - \frac{1}{6}\xi^2 + \frac{n}{120}\xi^4 + O(\xi^5)$$

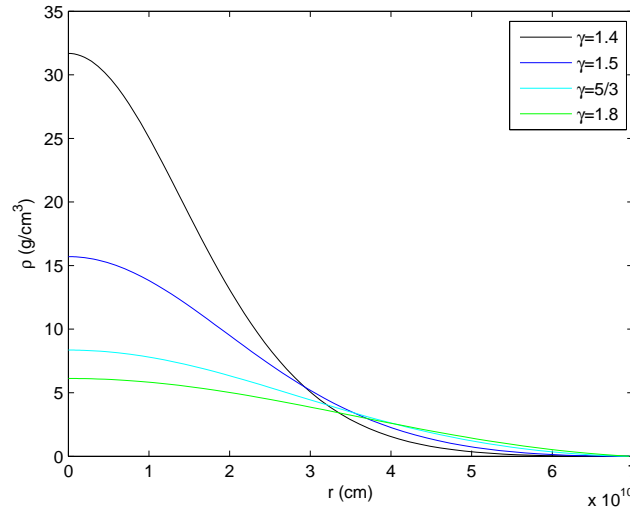


Figure 10: Density profile for stars with different γ , obtained by solving the Lane-Emden equation. Models that exhibit a high density core (black and blue) correspond to the structure of massive and evolved stars, like red giants. Models with a flatter density profile (green and cyan) correspond to lower mass stars and younger stars which had no chance to develop compact cores.

Solving the Lane-Emden equation starting at $\varepsilon = 2^{-45}$, and with initial conditions $\theta(\varepsilon) = 1 - \varepsilon/6$ and $\theta'(\varepsilon) = -\varepsilon/3$, we obtain the density profiles in Figure 10. In order to change from $x = \xi/\xi_1$ and θ to the cgs system of units, we will need to calculate ρ_c using that

$$M_* = 4\pi\rho_c \int_0^{R_*} \theta^n(r) r^2 dr$$

Let us consider a fluid element of the star, bounded to the BH, located within a disk at distance Δr from the center of the star, as it is shown in Figure 11. The specific potential energy in this disk is given by $\epsilon_p = -\frac{GM_{BH}}{R_p - \Delta r} = -\frac{GM_{BH}}{R_p} \left(1 - \frac{\Delta r}{R_p}\right)^{-1}$. Therefore,

$$-\frac{d\epsilon}{d\Delta r} = -\frac{GM_{BH}}{R_p^2} \left(1 - \frac{\Delta r}{R_p}\right)^{-2} \approx -\frac{GM_{BH}}{R_p^2} = -\frac{\Delta\epsilon}{R_*}$$

It is not difficult to show that

$$\frac{dM}{d\Delta r} = 2\pi \int_{\Delta r}^{R_*} \rho(r) r dr$$

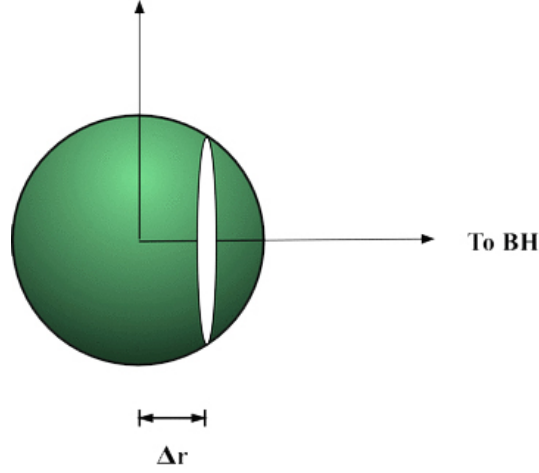


Figure 11: Schematic view of the star to show the geometry of the system. The radius of the star is R_* and the BH is in the right-hand side, at a distance $R_P \gg R_*$. Source: Lodato, King and Pringle, 2008 [16]

Finally,

$$\frac{dM}{d\epsilon} = \frac{dM}{d\Delta r} \frac{d\Delta r}{d\epsilon} = -\frac{dM}{d\Delta r} \frac{R_*}{\Delta\epsilon}$$

Using the new variables $x = \Delta r/R_*$, $m = M/M_*$ and $\tilde{\epsilon} = -\epsilon/\Delta\epsilon$, we obtain

$$\frac{dm}{d\tilde{\epsilon}} = \frac{dm}{dx} = 2\pi \int_x^1 \hat{\rho}(x') x' dx'$$

Although the energy distribution for $\epsilon > 0$ is irrelevant to compute \dot{M} , in order to compare it easily with Figure 7, we plot the whole distribution assuming it is symmetric. Energy distribution and the corresponding accretion rate curves can be found in Figure 12.

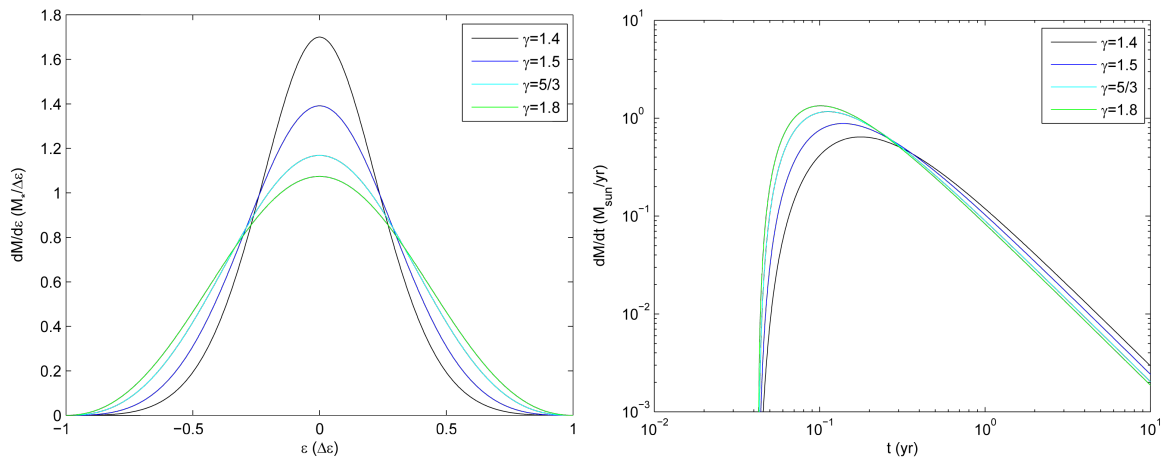


Figure 12: Mass distribution over specific orbital energy (left) and the corresponding accretion rate curves (right) for stars with different γ

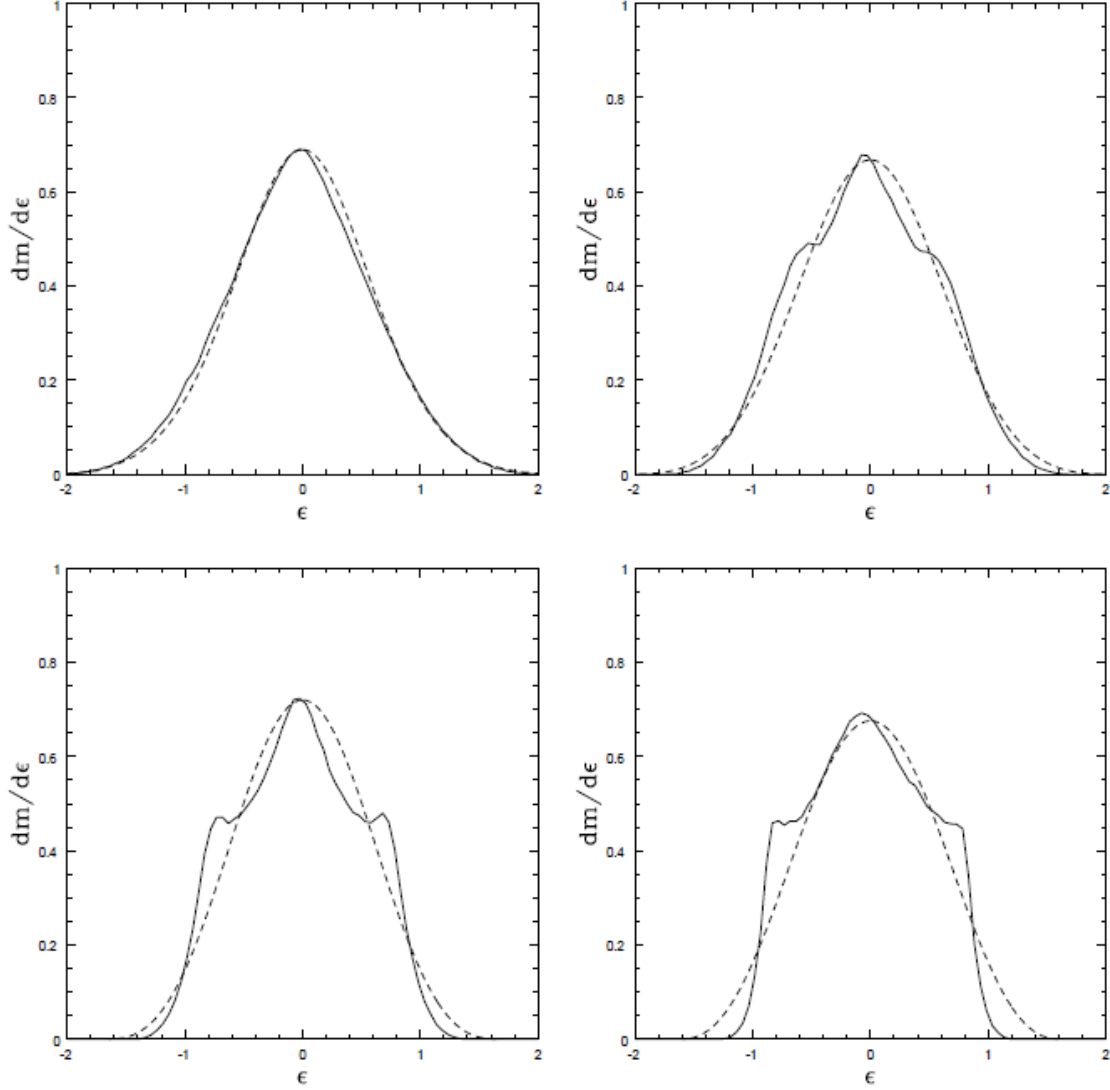


Figure 13: Specific orbital energy distribution using simulations (solid lines) and rescaled analytical solution (dashed lines), for $\gamma = 1.4$ (upper left), $\gamma = 1.5$ (upper right), $\gamma = 5/3$ (lower left) and $\gamma = 1.8$ (lower right). *Source: Lodato et al., 2008 [16]*

Comparison of energy distributions obtained analytically to those calculated from simulations (Lodato et al., 2008 [16]), reveals some differences. These arise because the analytic calculations assume that the disruption of the star is instantaneous once it reaches the tidal radius (which in our models corresponds to the pericenter of the orbit), while in reality the disruption begins earlier and the star is already somewhat inflated once it arrives to pericenter. This expansion can be taken into account by rescaling the radius by a factor ζ that depends on the polytropic index (see [16] for the values of ζ for different γ). The comparison between simulations and rescaled analytical solutions is shown Figure 13. We see that the curves differ more from one to another for large γ and equations of state that correspond to lower mass stars.

Once the distribution of specific orbital energy is known it is straight forward to rescale it for the

relativistic model and plot the accretion rate curves. The distribution of specific orbital energy and accretion curves for both models using $\gamma = 1.5$ are shown Figures 14 and 15.

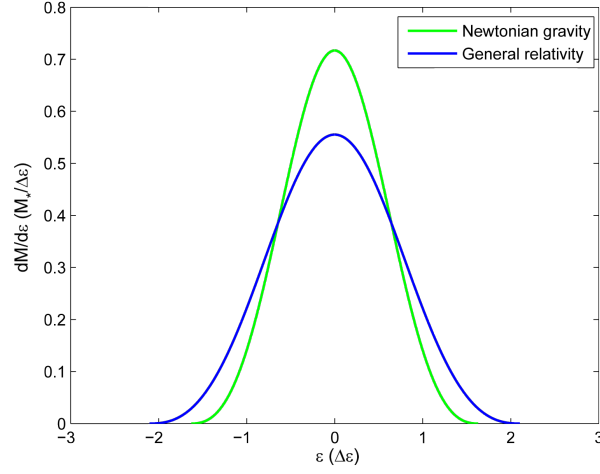


Figure 14: Distribution of the debris mass over specific orbital energy, for a star with $\gamma = 1.5$, disrupted in a Newtonian (green) and relativistic (blue) gravitational potential of a BH. Parameters of the encounter: $M_{BH} = 10^7 M_{\odot}$, $M_* = M_{\odot}$, $R_* = R_{\odot}$, $R_P = R_T = 5 R_g$.

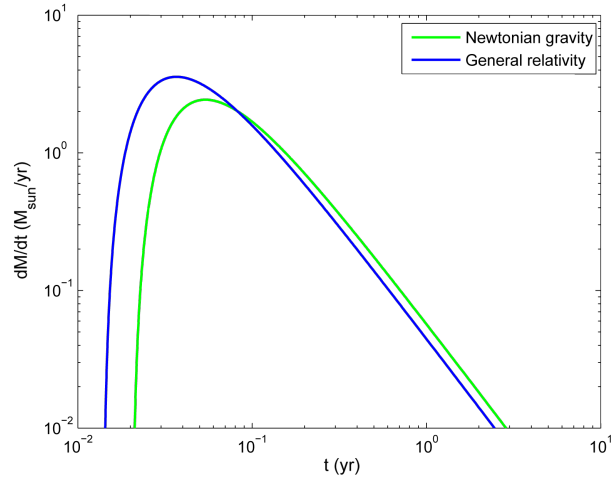


Figure 15: Accretion rate curve for Newtonian (green) and relativistic (blue) models. Same scenario as Figure 14.

5. Observational effects

As shown in Section 2.3, the accretion rate based on the simplest theoretical models is given by

$$\dot{M} = \frac{1}{3} \frac{M_*}{\tau_m} \left(\frac{\tau}{\tau_m} \right)^{-5/3}$$

where

$$\tau_m = \frac{\pi}{\sqrt{2GM_{BH}}} \frac{R_p^3}{R_*^{3/2}}$$

is the time scale for the most strongly bound debris to return to pericenter (i.e., its orbital period). Using $R_p = R_T = R_* (M_{BH}/M_*)^{1/3}$, one gets that $\tau_m \propto \sqrt{M_{BH}}$. It follows then that the width of the light curve will also be proportional to $\sqrt{M_{BH}}$, assuming that the returning debris promptly falls into the BH and that the luminosity closely corresponds to the BH accretion rate. Plots of \dot{M} for different BH masses can be seen in Figures 16 and 17. Figure 16 also includes the widths of the curves.

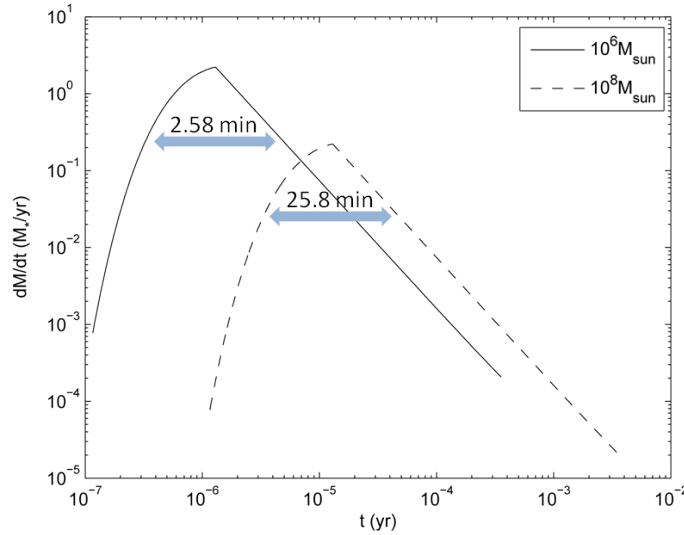


Figure 16: Plot of \dot{M} using $M_{BH} = 10^6 M_\odot$ (solid line) and $10^8 M_\odot$ (dashed line), $M_* = M_\odot$, $R_* = R_\odot$, $\beta = 1$ and $R_T = R_* (M_{BH}/M_*)^{1/3}$.

When observational data are analyzed, the moment in time at which the stellar disruption took place ($t = 0$ in our models) is not known, since accretion onto the BH starts after the period of time τ_m and the luminous outburst is delayed. A procedure to model the observed light curves of real TDEs therefore cannot rely on matching $t = 0$ for the data and models. Instead, a practice commonly used it to choose a model for a particular BH mass, and match the peak of light curve of the model with the observed light curve. In the next step, the width of the modeled light curve is “stretched” so that it corresponds to the data. Since the width of the light curve scales with BH mass, as described above, one can use the stretch factor applied to the model to infer the BH mass for the observed TDEs. Any relativistic effects are commonly neglected in this type of analysis and modeled light curves compared to the data are derived from purely Newtonian models.

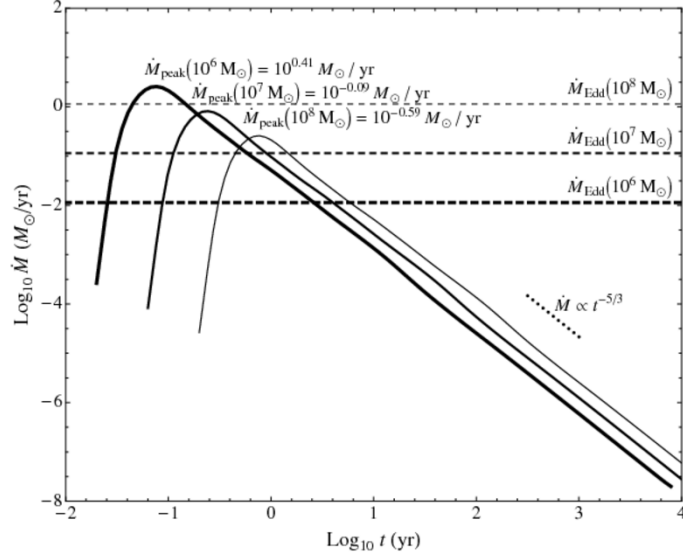


Figure 17: Simulations of accretion rates using $M_{\text{BH}} = 10^6 M_\odot$, $10^7 M_\odot$ and $10^8 M_\odot$, $\beta = 2$, and a star with structure similar to that of the Sun. *Source: De Colle et al., 2012 [12]*

The accretion rates of debris mass obtained for the scenario in Figure 7 ($M_{\text{BH}} = 10^7 M_\odot$, $M_* = M_\odot$, $R_* = R_\odot$, $R_T = R_P = 5 R_g$) are given in Figure 18. It can be seen that:

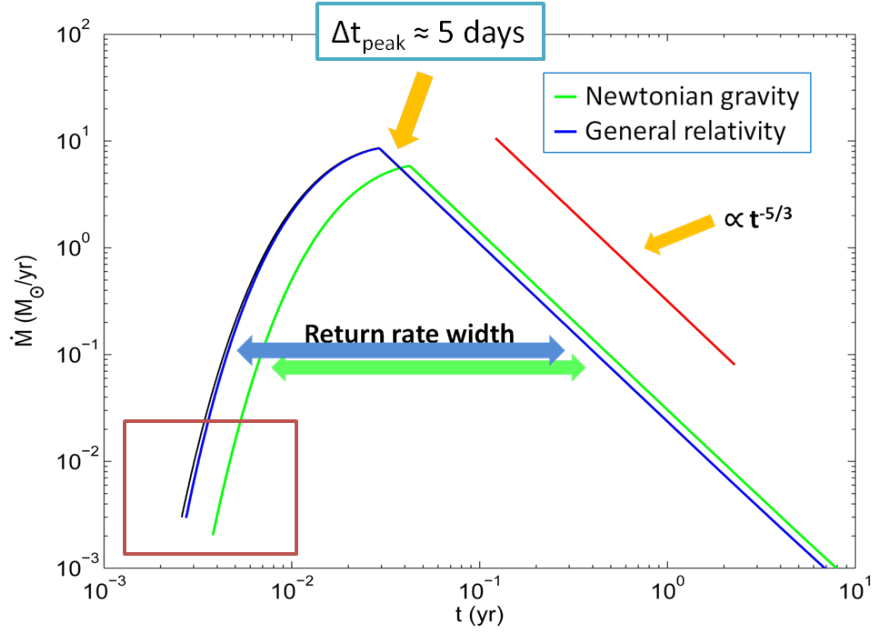


Figure 18: Return rate of debris mass in Newtonian and relativistic models. Same scenario as Figure 7.

- both Newtonian and relativistic models produce accretion rate $\propto t^{-5/3}$ at large t .

- the peak in the Newtonian curve occurs later than in the relativistic curve (in this scenario the delay is about 5 days). This delay arises from differences in the distributions of specific orbital energy for Newtonian and relativistic case. Note that some of the presently operating synoptic sky surveys image the sky with a cadence of 3 days, making delays of this order or longer detectable in principle.
- in addition to the offset in time, the width of the return rate curves is different for the Newtonian and relativistic model ($\text{width}_N/\text{width}_{GR} \approx 1.462$). Note that this implies that if an estimation of M_{BH} was attempted by modeling of the observed TDE light curve with a Newtonian model (with the same star characteristics and pericenter distance), that an error of $(\text{width}_N/\text{width}_{GR})^2 \approx 2.14$ would arise in the estimate of the BH mass due to a mismatch in models. Specifically, the mass of the BH inferred using the Newtonian model on a relativistic TDE would result in 2.14 times smaller M_{BH} estimate.
- the relativistic precession of the pericenter is not an important effect, in the sense that it does not significantly affect the shape of the light curve in our models. This is illustrated in Figure 19, which is a zoom-in of the region enclosed in the red box in Figure 18. We compare the accretion curves calculated with the relativistic model where precession is taken into account (blue) to that from a relativistic model where precession was neglected (black). The difference between the two models is small and below the detection limit of all astronomical transient surveys operating at present time. The relativistic precession of the pericenter however has an important consequence because it leads to collision of debris streams where hydrodynamic pressure forces can redistribute the debris orbits. Our analytic calculation however cannot capture the hydrodynamic effects and we discuss the implications of it for our results in the next section.

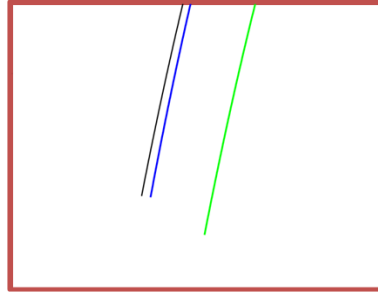


Figure 19: Zoom-in view of the beginning of the accretion rate curve in Figure 18. Black line shows the rate based on GR distribution while neglecting the pericenter precession, compared to the blue line which takes it into account.

6. Case study: Observed tidal disruption event, PS1-10jh

In this section we compare our models with the data obtained from a particular TDE candidate in order to estimate the physical parameters for this tidal disruption scenario. Specifically, we will use the data from a TDE candidate, PS1-10jh, which was discovered as an optical transient in May 2010 in the Pan-STARRS1 (PS1) Medium Deep Survey [6]. The transient was observed to coincide with the center of the host galaxy and exhibits light curves in several wavelength bands that are consistent with TDEs. Figure 20 shows the UV and optical light curves observed for this event over several years after disruption.

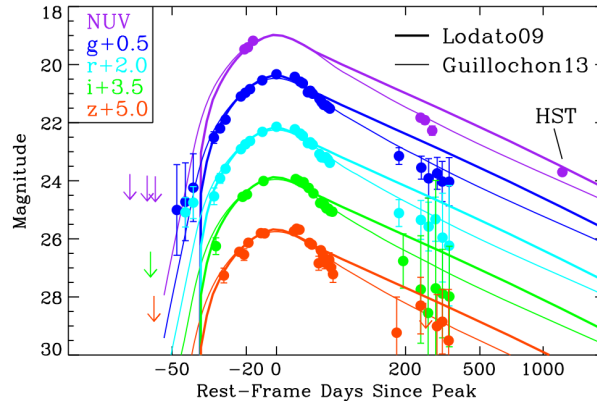


Figure 20: Light curves of the TDE candidate PS1-10jh, measured by GALEX in the near UV and Pan-STARRS1 in the g , r , i , z wavelength bands. Thin and thick lines mark two different models for the fallback rate used in the original publication. *Source: Gezari et al., 2015 [7].*

This event is of particular interest because it has been predicted that stellar disruption took place close to the BH, and hence, relativistic effects may be important [13], [14]. At present time, electromagnetic emission associated with this tidal disruption transient has faded out of sight and the only emission that can be observed in this location is that of the underlying host galaxy. Therefore, no new constraints on this tidal disruption scenario can be obtained from observations, leaving modelling as the only avenue for investigating its physical parameters.

6.1 Relating observed magnitudes and luminosities

As discussed in Section 2.3, in this work we assumed that $L \propto \dot{M}$, where L is the bolometric luminosity of a TDE. In observational astronomy, the brightness of an object is commonly measured in magnitudes. There are two different definitions of magnitude: the apparent magnitude m , that is the brightness of the object as we see it from Earth, and the absolute magnitude M , that is a reference brightness of the same object as it would appear if it was at a distance 10 pc away from Earth. The data of the TDE candidate PS1-10jh, obtained from <https://tde.space/>, is given in apparent magnitudes. The relation between these two definitions is

$$m = M - 2.5 \log_{10} \left(\frac{F_m}{F_M} \right)$$

where F_m is the flux detected on Earth and F_M is a reference flux. Therefore,

$$F_m = F_M \cdot 10^{0.4(M-m)} \propto 10^{-0.4m}$$

Assuming that the light is isotropically emitted, the relation between the luminosity and the flux at a distance d is given by $L = 4\pi d^2 F_m$, and hence, $\dot{M} \propto L \propto F_m \propto 10^{-0.4m}$. We will use this relationship to transform the brightness of PS1-10jh given as apparent magnitude into $10^{-0.4m}$, a property that can be compared with the mass accretion rate estimated in our theoretical models.

6.2 Estimation of BH mass in PS1-10jh

When observed data are studied, the moment of stellar disruption is generally not known. The way that M_{BH} and t_{disr} (time when the disruption took place, taking $t = 0$ as the peak of the curve) are commonly estimated is by matching the peak of the data with the peak of the modeled accretion curve for a particular M_{BH} . Then, by scaling M_{BH} in the model, the width of the model curve is matched to the data. As discussed in Section 5, Newtonian models are usually used to estimate M_{BH} in TDE candidates. In this project the data will be compared with the models for different M_{BH} and t_{disr} . We will consider only the data obtained in the g (optical) band because the light curve is sampled by a maximum number of points with smaller error bars relative to the other spectral bands. Similar results should however be obtained by considering other bands.

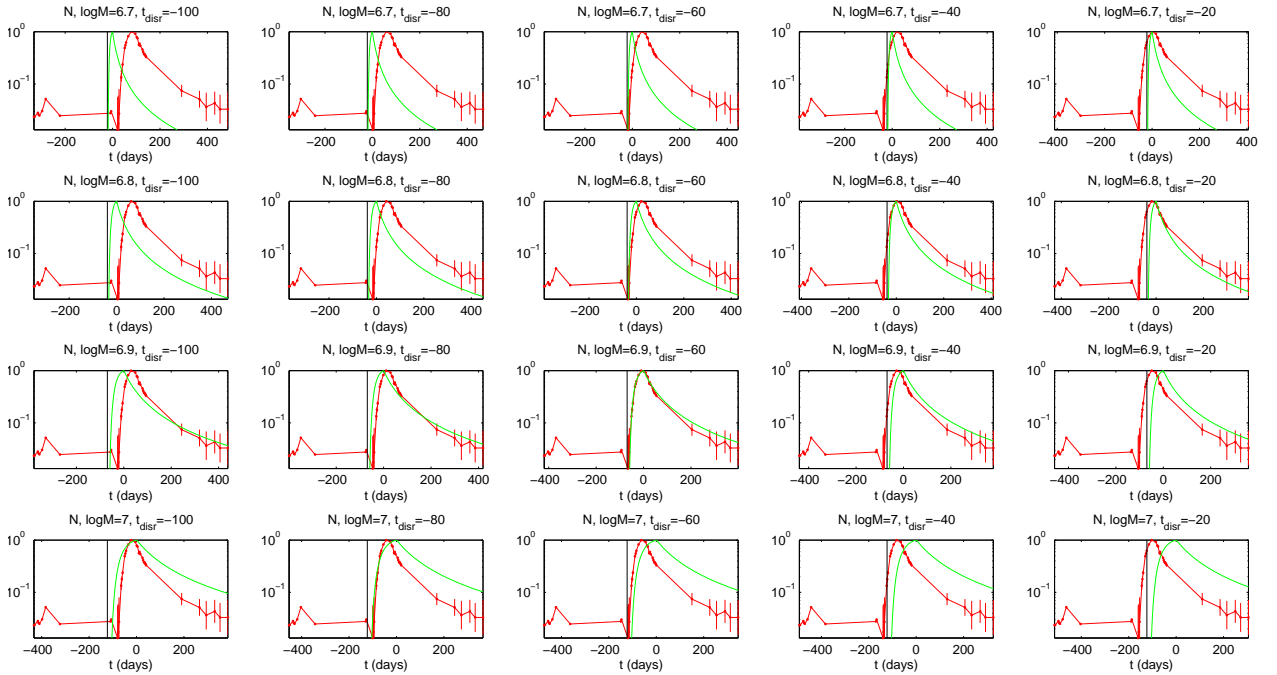


Figure 21: Visual comparison of the g -band data of PS1-10jh (red data points with error bars and lines) and the Newtonian model of tidal disruption (green), for different M_{BH} (in M_\odot) and t_{disr} (in days). Black vertical line indicates the moment of disruption in the model. For the tidal disruption model curves we assume $M_* = M_\odot$, $R_* = R_\odot$ and $R_p = R_T = 10R_g$.

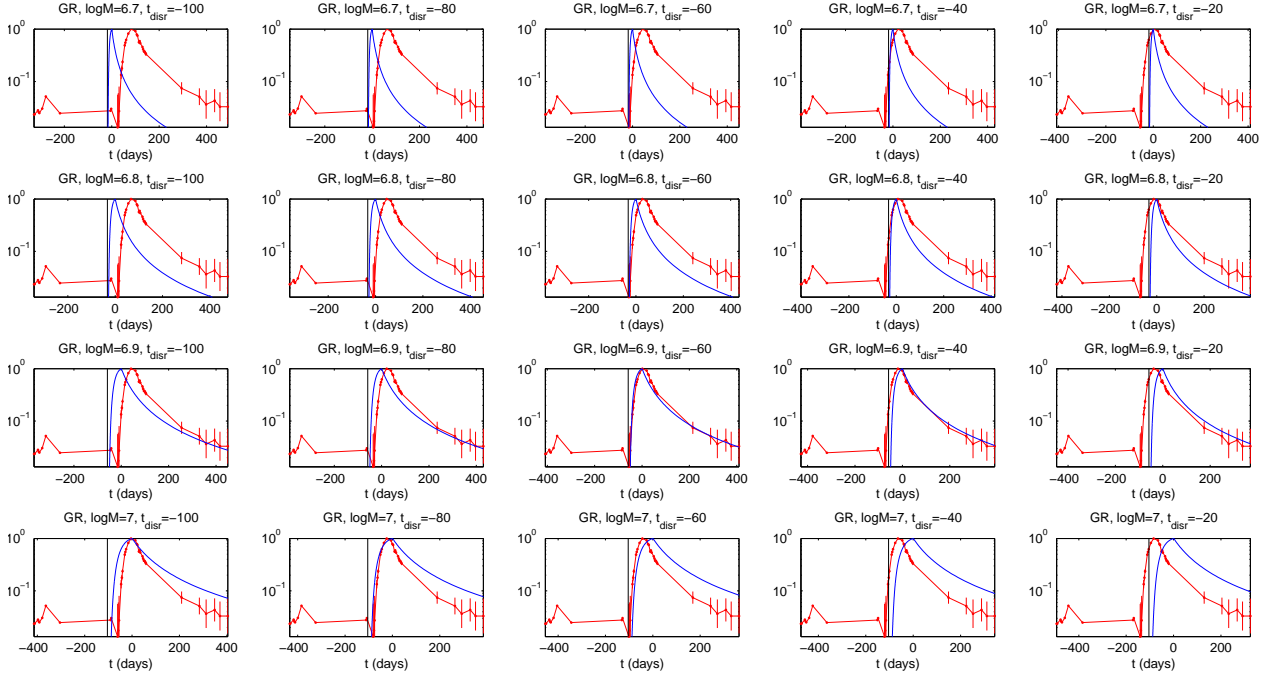


Figure 22: Visual comparison of the g -band data of PS1-10jh (red data points with error bars and lines) and the relativistic model of tidal disruption (blue), for different M_{BH} (in M_{\odot}) and t_{disr} (in days). Black vertical line indicates the moment of disruption in the model. For the tidal disruption model curves we assume $M_* = M_{\odot}$, $R_* = R_{\odot}$ and $R_P = R_T = 10R_g$.

Figures 21 and 22 provide a visual illustration of the models based on simple energy distributions similar to Figure 7 and the data for PS1-10jh. In order to plot them on the same scale, both the observed light curve and the modeled accretion rate curve are normalized to 1. While plots are useful for visual comparison, a quantitative method is needed in order to identify the best fit. In order to do that, we calculate a grid of models and evaluate the χ^2 statistic,

$$\chi^2 = \frac{(L_{model} - L_{observed})^2}{L_{model}}$$

for every comparison with the observed light curve. The best fit is identified by the smallest χ^2 [18]. The plots of χ^2 calculated for Newtonian and relativistic models can be seen in Figure 23.

The minimum χ^2 are close to 1 and correspond to $M_{BH,N} = 10^{6.8938} M_{\odot} \approx 7.83 \cdot 10^6 M_{\odot}$ and $t_{disr,N} = -58.75$ days for the Newtonian model and $M_{BH,GR} = 10^{6.9375} M_{\odot} \approx 8.66 \cdot 10^6 M_{\odot}$ and $t_{disr,GR} = -62.02$ days for the relativistic model. As expected, the estimated M_{BH} is higher in the relativistic model than in the Newtonian model ($M_{BH,GR}/M_{BH,N} \approx 1.106$). The plots for the best fits are given in Figure 24.

The difference of about 10% is relatively small considering the precision of a variety of methods used to estimate BH masses from astronomical observations. However, for increasingly closer encounters, the difference between the Newtonian and relativistic models should increase. Figure 25 illustrates this effect and shows the estimated BH mass as a function of the tidal radius, $R_T = R_P$, for $\beta = 1$ encounters. Since in both models we assume that a disrupted star is Sun-like ($M_* = M_{\odot}$, $R_* = R_{\odot}$), the different values

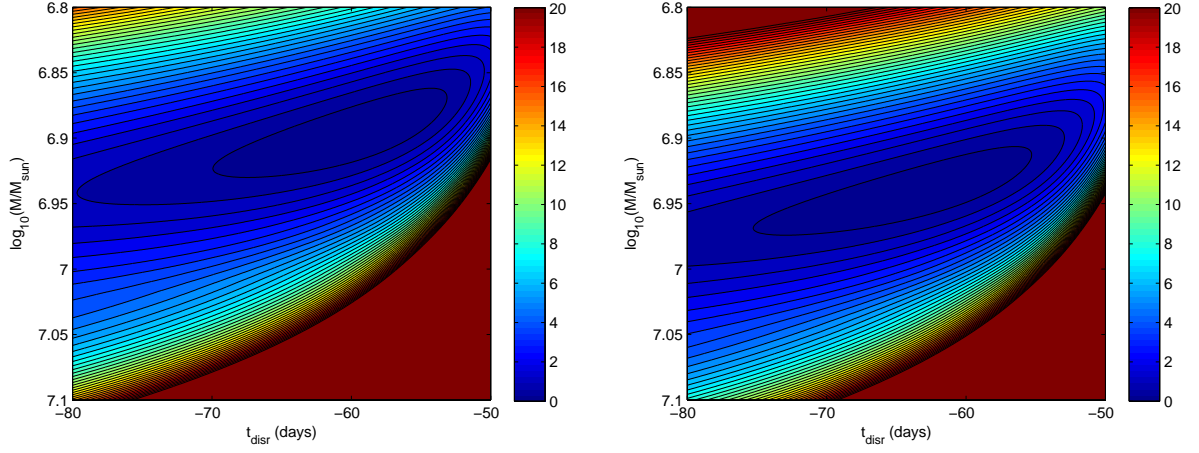


Figure 23: Contour plot of χ^2 for different M_{BH} (in M_\odot) and t_{disr} (in days) using the Newtonian (left) and relativistic (right) models. In both models we assume that $M_* = M_\odot$, $R_* = R_\odot$ and $R_P = R_T = 10R_g$.

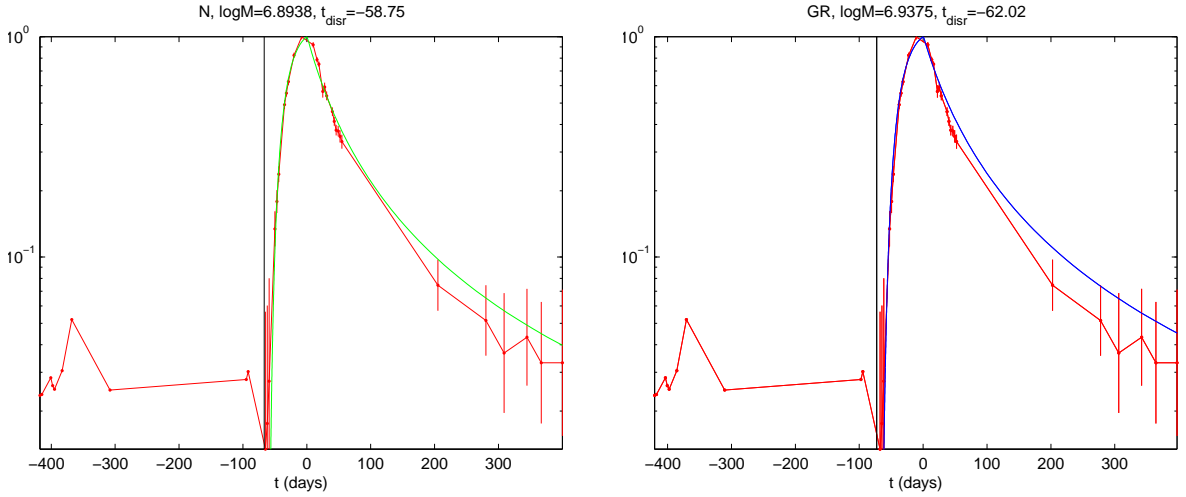


Figure 24: Data from PS1-10jh with the best fits for newtonian (left) and relativistic (right) models. In both models we assume that $M_* = M_\odot$, $R_* = R_\odot$ and $R_P = R_T = 10R_g$.

of tidal radius would correspond to a disruption of stars with different inner structure. For example, stars disrupted at the tidal radius of $6 R_g$ would have evolved to have more compact cores than stars disrupted at $10 R_g$.

When we repeat the same analysis for the models where the distribution of debris energy is obtained by solving the Lane-Emden equation, we find that the modeled accretion rate curves provide a poor match for the ones observed from PS1-10jh. This is illustrated in Figure 26 which shows that the modeled light curves exhibit an abrupt rise to the peak in the accretion rate and a more gradual decline after it, which provide a poor match for the shape of the observed light curve. This is true for both the Newtonian and

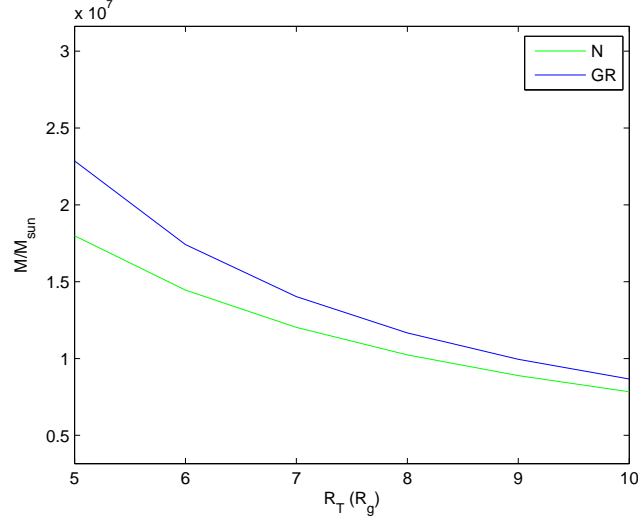


Figure 25: Best fit of M_{BH} as a function of tidal radius assuming stellar disruption at the pericenter of the orbit ($\beta = 1$ encounter).

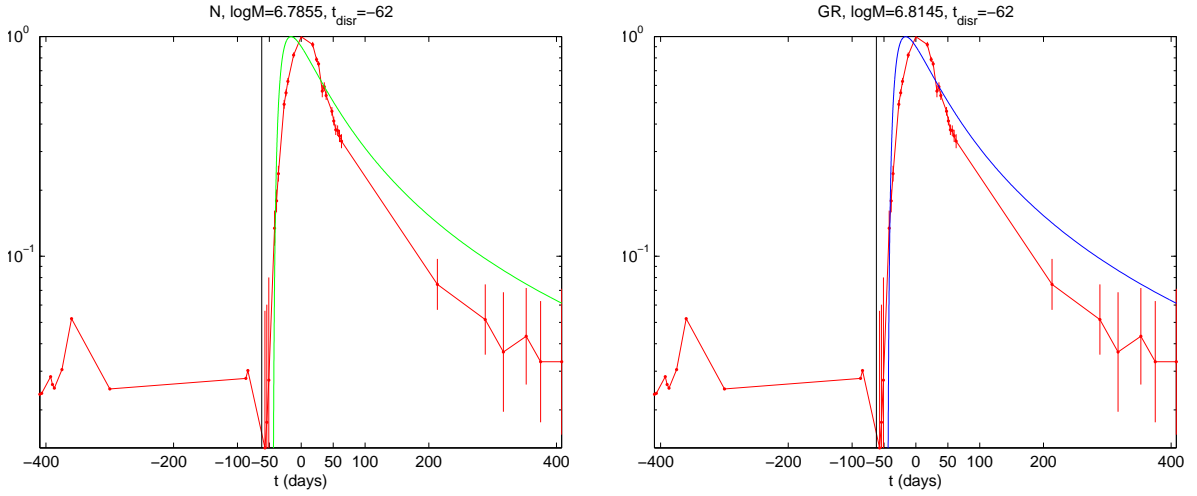


Figure 26: Data from PS1-10jh with the best fits for newtonian (left) and relativistic (right) models. In both models we assume that $M_* = M_\odot$, $R_* = R_\odot$ and $R_p = R_T = 10R_g$.

relativistic models and arises from the fact that the modeled energy distributions shown in Figure 12 are relatively narrow and do not take into account tidal interaction of the star with the BH before it arrives to pericenter. Therefore, we do not further consider this family of models.

7. Conclusions

The light curves from TDEs encode information about the scenario in which the disruption happened. Therefore, it is useful to understand how are they produced. The main result of this study is that for a relativistic tidal disruption that occurs at a given tidal radius modeling the light curve with relativistic models returns a larger value for the BH mass than if the Newtonian models are used. We also find that the magnitude of this effect increases for closer encounters of stars with BHs and therefore, relativistic TDEs misidentified as Newtonian encounters inevitably lead to an error in the estimate of the BH mass.

Although the distributions of debris over the specific orbital energy assumed in Section 6 are simpler than the ones obtained solving the Lane-Emden equation, the accretion rate curves obtained with such simple distributions match better with the observed light curve of PS1-10jh. As discussed in the previous section, the reason is that energy distributions based on the Lane-Emden equation include an implicit assumption that disruption occurs at pericenter, whereas in real TDEs the disruption actually starts before the star reaches the pericenter.

The analytic models presented in this project rely on certain approximations. We assume that every fluid element travels on an orbit that does not interact with the rest of the debris. This is almost certainly an over-simplification. After stellar disruption, orbits of fluid elements will intersect and experience collisions, mediated by fluid pressure forces. Collisions redistribute orbital energy among the fluid elements, modifying the original energy distribution along the way. The hydrodynamic effects of this nature are beyond the analytic models used here and can only be captured in hydrodynamic simulations.

For example, hydrodynamics simulations described by Cheng and Bogdanović (2014) [9] predict a different behavior of the TDE accretion curves in presence of general relativistic effects. In this case the peak in the accretion rate occurs later in relativistic than in Newtonian simulations, a conclusion opposite from the analytic models (see Figure 27 from their work). In addition, the light curves appear broader in the relativistic model, as it can be seen in the right panel of Figure 27, based on a simulation of tidal disruption of a white dwarf star.

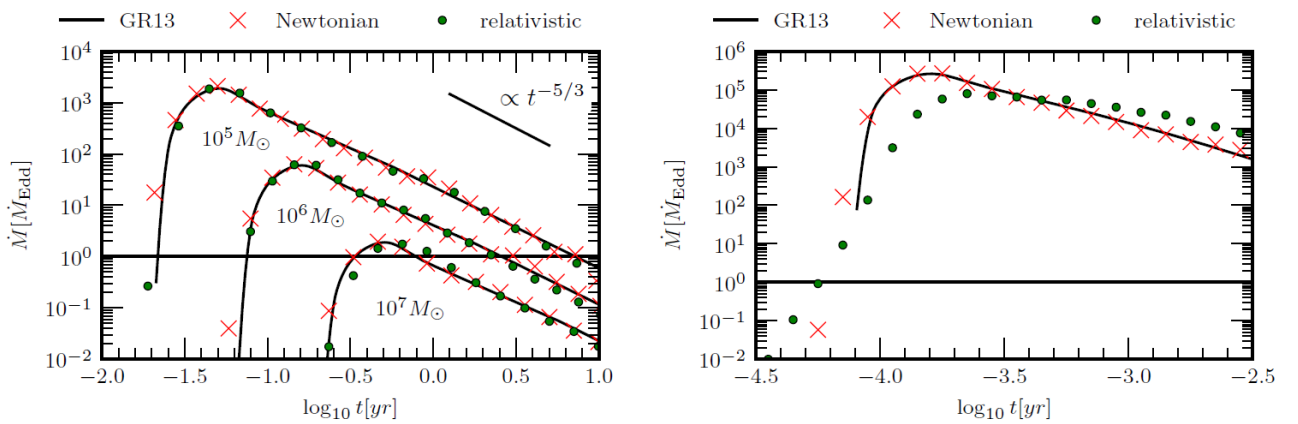


Figure 27: Accretion rates for simulations from different scenarios, using newtonian (red \times) and relativistic models (green circles), compared with parametric fits from [15] (solid line). Left (low mass main sequence star): $M_{BH} = 10^5 M_{\odot}, 10^6 M_{\odot}$ and $10^7 M_{\odot}$, $M_* = M_{\odot}$, $M_* = M_{\odot}$, $\gamma = 5/3$ and $\beta = 1$. Right (white dwarf): $M_{BH} = 10^5 M_{\odot}$, $M_* = 0.6 M_{\odot}$, $R_* = 1.51 \cdot 10^{-2} R_{\odot}$, $\gamma = 5/3$ and $\beta = 0.784$. Source: Cheng and Bogdanović, 2014 [9]

This behavior arises because collisions of debris streams actually delay accretion onto the BH. The collisions are more important when relativistic effects are considerable, due to pericenter precession. Since orbits of fluid elements deep in the potential well of the BH precesses at different rates, collisions are prevalent and hence, it is more important to take them into account. Therefore, hydrodynamic effects and stream-stream collisions play a very important role in the relativistic scenario and must be considered in order to make accurate predictions for the TDE light curves.

References

- [1] J. Guillochon, *Astrocraash.net: The research of James Guillochon - Tidal Disruption of Stars by Black Holes*, <https://astrocrash.net/projects/tidal-disruption-of-stars/>
- [2] C.R. Evans, C.S. Kochanek, *Tidal disruption of a star by a massive black hole*, The Astrophysical Journal, L13-L16, 346 (1989)
- [3] M.J. Rees, *Tidal disruption of stars by black holes of $10^6 - 10^8$ solar masses in nearby galaxies*, Nature, vol. 333, 523 (1988)
- [4] N.C. Stone, B.D. Metzger, *Rates of Stellar Tidal Disruption as Probes of the Supermassive Black Hole Mass Function*, arXiv:1410.7772 (2016)
- [5] S. Komossa, *Tidal disruption of stars by supermassive black holes: Status of observations*, arXiv:1505.01093 (2015)
- [6] S. Gezari et al., *An ultraviolet-optical flare from the tidal disruption of a helium-rich stellar core*, Nature, 485, 217 (2012)
- [7] S. Gezari et al., *PS1-10jh continues to follow the fallback accretion rate of a tidally disrupted star*, The Astrophysical Journal Letters, 815:L5 (2015)
- [8] J.B. Hartle, *Gravity: An Introduction to Einstein's General Relativity*, Pearson Education (2003)
- [9] R.M. Cheng, T. Bogdanović, *Tidal disruption of a star in the Schwarzschild spacetime: relativistic effects in the return rate of debris*, arXiv:1407.3266 (2014)
- [10] J. Servin, M. Kesden, *A unified treatment of tidal disruption by Schwarzschild black holes*, arXiv:1611.03036 (2016)
- [11] C. Evans, P. Laguna, M. Eracleous, *Ultra-close encounters of stars with massive black holes: tidal disruption events with prompt hyperaccretion*, The Astrophysical Journal Letters 805:L19 (2015)
- [12] F. De Colle, J. Guillochon, J. Naiman, E. Ramirez-Ruiz, *The dynamics, appearance and demographics of relativistic jets triggered by tidal disruption of stars in quiescent supermassive black holes*, arXiv:1205.1507 (2012)
- [13] J. Guillochon, H. Manukian, E. Ramirez-Ruiz, *PS1-10jh: The disruption of a main-sequence star of near-solar composition* The Astrophysical Journal, 783:23 (2014)
- [14] T. Bogdanović, R.M. Cheng, P. Amaro-Seoane, *Disruption of a red giant star by a supermassive black hole and the case of PS1-10jh*, The Astrophysical Journal, 788:99 (2014)
- [15] J. Guillochon, E. Ramirez-Ruiz, *Hydrodynamical simulations to determine the feeding rate of black holes by the tidal disruption of stars: the importance of the impact parameter and stellar structure*, The Astrophysical Journal, 767:25 (2013)
- [16] G. Lodato, A.R. King, J.E. Pringle, *Stellar disruption by a supermassive black hole: is the light curve really proportional to $t^{-5/3}$?*, arXiv:0810.1288 (2008)

- [17] M. Kesden, *Black-hole spin dependence in the light curves of tidal disruption events*, arXiv:1207.6401 (2012)
- [18] J.V. Wall, C.R. Jenkins, *Practical Statistics for Astronomers*, Cambridge University Press (2003)